

Cite this: *J. Mater. Chem. C*, 2021,
9, 14421

High-performance cement/SWCNT thermoelectric nanocomposites and a structural thermoelectric generator device towards large-scale thermal energy harvesting†

Ioanna Vareli,^a Lazaros Tzounis,^b Kyriaki Tsirka,^a Ioannis E. Kavvadias,^c Konstantinos Tsongas,^c Marco Liebscher,^d Anaxagoras Elenas,^c Leonidas N. Gergidis,^a Nektaria-Marianthi Barkoula^a and Alkiviadis S. Paipetis^{*a}

For the first time, the thermoelectric properties of cement/single-walled carbon nanotube (SWCNT) nanocomposites with over 3, 7, 14 and 28 days of hydration are reported, while a thermoelectric generator device (TEG) is fabricated utilising the material with the highest achieved power factor (PF). SWCNTs with inherent p-type semiconductor characteristics were introduced into the cementitious matrix at a water to cement (w/c) ratio of 0.5, while the Seebeck coefficient (S), electrical conductivity (σ) and PF for different SWCNT loadings were determined at different ages. The 28 day cement/SWCNT sample with 0.5 wt% loading exhibited the highest performance in terms of σ ($1.59 \times 10^3 \text{ S m}^{-1}$), S ($+1348.8 \mu\text{V K}^{-1}$) and PF ($2.89 \times 10^3 \mu\text{W m}^{-1} \text{ K}^{-2}$), with the PF being the highest among other carbon nanoadditive-based cement thermoelectric nanocomposites to date. The cement/SWCNT(0.5) was used for the fabrication of a thermoelectric generator (TEG) device exhibiting a maximum power output (P_{max}) of $5.02 \mu\text{W}$ and a power density of 5.02 mW m^{-2} , upon being exposed to a temperature difference (ΔT) of 50 K. Finite element (FE) simulations validated the TEG thermoelectric performance corroborating the experimental findings. The highly efficient cement/SWCNT thermoelectric nanocomposites, as well as the cement-based structural TEG device, demonstrated herein could open new avenues towards future energy efficient buildings and green construction.

Received 27th July 2021,
Accepted 16th September 2021

DOI: 10.1039/d1tc03495b

rsc.li/materials-c

1. Introduction

Over the last few decades, expanding demand for alternative energy resources has emerged due to the finite amount of fossil fuels and the anthropogenic global climate change. To that end, it is worth mentioning that more than 60% of the global energy production is dissipated as waste heat and as a result, it is impractical to be fruitfully utilized.¹ In terms of sustainable construction technologies, thermoelectric materials have become one of the potential candidates for thermal energy harvesting due to their ability to convert waste heat energy into electricity.²

Thermoelectric materials conform to the common thermoelectric or Seebeck effect illustrated by the Seebeck coefficient (S), or thermoelectric power (TEP), which is the direct solid state conversion of thermal energy to electrical energy.³ The Seebeck coefficient (in units of $\mu\text{V K}^{-1}$) is the open circuit potential (V_{oc}) or the generated thermovoltage per unit temperature difference (ΔT) between a hot and cold point, expressed by the following equation (eqn (1)):

$$S = \frac{\Delta V}{\Delta T} \quad (1)$$

The Seebeck coefficient is employed for the calculation of the power factor ($\text{PF} = S^2\sigma$), a commonly used entity for the comparison of thermoelectric materials' efficiency. Till now, mainly inorganic low band-gap semiconductors such as Bi_2Te_3 ⁴ and SnSe ⁵ have been used for thermoelectric generator (TEG) devices, while it could be easily realised that their wide-spread application is hindered by their relatively high cost, consisting of rare and toxic elements, *etc.*⁶ It is worth noting that a recent review could be found where inorganic, organic and inorganic/organic hybrid fiber-based thermoelectrics and TEG devices

^a Department of Materials Science & Engineering, University of Ioannina, GR-45110 Ioannina, Greece. E-mail: latzounis@uoii.gr

^b Mechanical Engineering Department, Hellenic Mediterranean University, Estavromenos, 71004 Heraklion, Greece. E-mail: tzounis@hmu.gr

^c Department of Civil Engineering, Democritus University of Thrace, GR-67100, Xanthi, Greece

^d Technische Universität Dresden, Institute of Construction Materials, DE-01062 Dresden, Germany

† Electronic supplementary information (ESI) available. See DOI: 10.1039/d1tc03495b

have been thoroughly summarised focusing on the synthesis, characterization, fundamentals, property evaluation, and elaborating possible practical applications *i.e.* for solid, portable, and wearable electronics.⁷ In a more focused review article, fiber based thermoelectrics have been comprehensively summarized elucidating the state-of-the-art of fiber-based thermoelectric materials and TEG devices made thereof, while considering their important aspects; namely, (i) novel chemical protocols and chemical engineering, (ii) achievement of outstanding thermoelectric material properties based on specific energy level mechanisms, (iii) advanced TEG device fabrication methods and unique designs of wearable TEGs, (iv) device flexibility, stability and performance, and (v) their potential practical applications.⁸

Concrete and other cement-based composites are the most commonly used materials for construction and buildings with almost 2.5 tons of concrete consumed per person annually.⁹ Advanced energy efficiency in buildings is a crucial feature determining human-induced emissions worldwide, while state-of-the-art materials for advancing large-scale ambient thermal energy harvesting have been the spotlight in applied energy research.¹⁰ The thermoelectric effect in buildings and other civil engineering structures has been reported in the form of thermoelectric heat generation, as well as thermoelectric cooling.¹¹ The thermoelectric effect for cement-based materials permits a fascinating potential application in ambient energy harvesting, which could capture inaccessible ambient heat energy found in various locations, for example, buildings, urban area and roads, industrial environments, *etc.*, and convert it into usable electrical energy. Moreover, thermoelectric cement-based structural materials can capture waste heat in urban areas, highways, railway infrastructure and buildings currently contributing to the Urban Heat Island (UHI). Additionally, thermoelectric cement-based structural materials set the ground towards exploiting huge wasted amounts of heat found in concrete structures.¹² Such structures are exposed to temperature and light, generating heat that is currently lost *via* waste heat in the environment. A fraction of that heat can be captured and reused for electricity generation.¹³

The thermoelectric effect in cement-based materials was first introduced by Sun *et al.* in 1998 in cement paste with short carbon fibers.¹⁴ The thermoelectric performance of carbon and steel fiber reinforced cement composites with Seebeck coefficients of about +5.5 and +68.0 $\mu\text{V K}^{-1}$ for carbon and steel fiber reinforced cement composites was reported by Wen and Chang respectively with a fiber content of 1.0% by mass of composite.^{15,16} More recently, they went deeply in the discussion about the origin of the thermoelectric behaviour in cement pastes reinforced with steel and carbon fibers.¹⁷ In another study, an enhanced Seebeck coefficient from +5.5 to +21.2 $\mu\text{V K}^{-1}$ was reported after the intercalation of bromine-carbon fibers instead of ordinary polyacrylonitrile fibers as reinforcement in hardened cement paste.¹⁸

The addition of 0.5 wt% multi-walled carbon nanotubes (MWCNTs) in carbon fiber/cement composites increased further the Seebeck coefficient reaching the highest value of +23.5 $\mu\text{V K}^{-1}$.¹⁹ Furthermore, an absolute Seebeck coefficient

reaching +127 $\mu\text{V K}^{-1}$ was reported by Demirel and Yazicioglu in carbon fiber reinforced concrete with the aid of silica fume.²⁰ Jin and Zhang *et al.* have reported an order of magnitude higher Seebeck coefficient compared to those of all existing studies related to thermoelectric cement composites. Namely, they reached values between +2500 and +3300 $\mu\text{V K}^{-1}$ by the addition of Fe_2O_3 and ZnO nanopowder in the cement matrix.²¹

In a recent study, Rudradawong *et al.* reported on Mayenite $\text{Ca}_{12}\text{Al}_{14}\text{O}_{33}$ /nano-carbon black composites (C12A7/nCB) elucidating the mechanism of positive ionic transport in thermoelectric properties. Specifically, the figure of merit, defined as $ZT = (S^2\sigma)T/\kappa$ where T , S , σ , and κ are absolute temperature, Seebeck coefficient, electrical, and thermal conductivity, respectively, for thermoelectric materials of C12A7/nCB of 10 wt% content was 0.16×10^{-3} , while the PF was in the range of 0.02 to 0.24 $\mu\text{W m}^{-1} \text{K}^{-2}$ with the Seebeck coefficient being +7 to +25 $\mu\text{V K}^{-1}$ in the temperature range of 300 to 380 K.²² Moreover, expanded graphite/carbon fibers reinforced cement (EG-CFRC) with a porosity of 3.9% showed a maximum of PF of $7.26 \times 10^{-4} \mu\text{W m}^{-1} \text{K}^{-2}$, while ZT was recorded to be 2.22×10^{-7} .²³ The thermoelectric properties of expanded graphite/carbon fiber-reinforced cement composites (EGCFRCs) were also investigated exhibiting a PF of $94.3 \mu\text{W m}^{-1} \text{K}^{-2}$ and a ZT of 2.208×10^{-3} when filled with ionic liquid 1-butyl-3-methylimidazolium bromide (IL [Bmim]Br).²⁴

Graphene has also been employed as a thermoelectric nanoadditive in cement towards highly efficient thermoelectric nanocomposites. Graphene nanoplatelets (GNPs) have been recently reported in a study by Ghosh *et al.* as inclusions in cement towards energy harvesting in buildings.²⁵ With a GNP loading of 15 wt%, an electrical conductivity of 16.2 S cm^{-1} and a Seebeck coefficient of +34 $\mu\text{V K}^{-1}$ were reported. For the time being, nanostructured graphene/zinc oxide hybrid cement composites exhibit the highest value of $ZT \sim 0.01$ acquired at 70 °C with 10 wt% graphene and 10 wt% ZnO inclusions, whereas the Seebeck coefficient obtained was +141 $\mu\text{V K}^{-1}$.²⁶

One of the most promising carbon nano-allotropes for thermoelectric energy harvesting, as well as for thermoelectric generator (TEG) devices, is carbon nanotubes (CNTs),^{27–30} amongst other organic *e.g.* small molecule and polymeric based semiconductors³¹ that have been summarised in a recent review article.³² Moreover, a recent article could be found where all the advancements regarding thermoelectric carbon allotrope materials and hybrids with inorganic crystals have been thoroughly reviewed, while reporting on carbon allotrope-hybrid related thermoelectric module design and possible practical applications.³³

CNTs have been long-established to enhance the mechanical and electrical properties of cementitious materials, while their electrical conductivity has been employed in structural health monitoring (SHM) applications, for strain-damage sensing, electromagnetic shielding effectiveness, *etc.*³⁴ Inside a cementitious matrix, CNTs form a network where charge carriers, electrons (n-doping) and holes (p-doping) are moving through a tunneling or a hopping transport mechanism,^{35,36} while simultaneously phonon scattering phenomena occur at the cement particle–CNT interfaces resulting in relatively low thermal conductivities. Consequently, CNT/cement nanocomposite

materials are considered as ideal candidates for thermoelectric power generation, while there is continuous scientific interest to increase the electrical conductivity, Seebeck coefficient and power factor values.

The thermoelectric properties of CNT reinforced cement nanocomposites were reported by Wei *et al.* reaching a Seebeck coefficient of $+57.98 \mu\text{V K}^{-1}$ and a comparatively high electrical conductivity of 0.818 S cm^{-1} .³⁷ Recently, Tzounis *et al.* reported on p- and n-type cement/MWCNT thermoelectric nanocomposites with the highest ever reported PF of cement/CNT thermoelements of $1.44 \mu\text{W m}^{-1} \text{ K}^{-2}$ before drying and $7.63 \times 10^{-3} \mu\text{W m}^{-1} \text{ K}^{-2}$ at 1.0 wt% of CNT filler. This is the only existing study that has elucidated the thermoelectric mechanisms and the effect of humidity/moisture at different cement ages, while a p-n TEG device demonstrator was shown consisting of a single p-n pair of serially interconnected cement/CNT thermoelements.³⁸ TEG devices based on the constructed thermoelectric materials are the only viable way of harvesting thermoelectric energy on a large scale *i.e.* in roads, pavements, and buildings' wasted thermal energy, while being able to deliver high power outputs for potential practical applications.

In the study at hand, cement/SWCNT nanocomposites at different SWCNT loadings have been prepared and utilised, for the first time, towards the fabrication of a TEG device consisting of ten (10) serially interconnected p-type thermoelements. Distinct emphasis is made on the influence of SWCNT loading, varying from 0.005 wt% to 0.5 wt% by cement's mass, on the thermoelectric performance of cement/SWCNT nanocomposites at different ages *i.e.*, 3, 7, 14 and 28 days in the direction of figuring out the relationship between the structure and the physical properties. The cementitious based TEG device produced a voltage output of 31.05 mV with a maximum power (P_{max}) of 5.02 μW , upon being exposed to a through-thickness thermal difference of $\Delta T = 50 \text{ K}$. This is the highest ever reported voltage and power output of a cementitious based TEG device. The experimental results were validated using finite element (FE) modelling for the solution of the coupled constitutive equations describing the underlying thermoelectric phenomena. The fabrication of cementitious TEG devices with a higher amount of p-type or alternating p-n serially interconnected thermoelements could allow further the increase of the total voltage and power output values.

2. Experimental

2.1 Materials

SWCNTs in powder form were provided by OCSiAl (TUBALL, carbon content: $>85 \text{ wt\%}$, mean diameter of $1.8 \pm 0.4 \text{ nm}$, length $>5 \mu\text{m}$, metal impurities $<15 \text{ wt\%}$). SDBS (Sodium dodecylbenzene sulfonate) was purchased from Sigma Aldrich to ensure adequate dispersion of SWCNTs. A commercially available poly-carboxylate (PCE) based superplasticizer (Viscocrete ultra-600) was purchased from Sika Hellas S.A., Greece to ensure sufficient workability of the cement/SWCNT slurries. Ordinary Portland cement (OPC) CEM I 42.5 R has been provided by

TITAN S.A. GREECE. Deionized water was used to prepare all nanocomposites in this study.

2.2 Fabrication of SWCNT bucky paper films

SWCNTs in the form of bucky papers were prepared for the investigation of their intrinsic electrical and thermoelectric properties (Fig. 1). Following a vacuum filtration process through a polycarbonate membrane ($0.4 \mu\text{m}$ pore size), the bucky papers were fabricated from previously prepared stable SWCNT/water dispersions at a concentration of 20 mg ml^{-1} and 1:1 ratio of SDBS surfactant to SWCNTs by mass ($\sim 150 \text{ mg}$ of SWCNT powder was used for the bucky paper preparation). The final bucky paper films were derived *via* a vacuum filtration process, peeled off from the membrane and the thickness was measured to be approximately $\sim 80 \mu\text{m}$.

2.3 Preparation of cement/SWCNT paste and nanocomposite specimens

For the dispersion of SWCNTs in DI water, SDBS, an anionic surfactant was employed. The stock solution/dispersions contained a predetermined amount of SWCNTs of 0.005 wt%, 0.01 wt%, 0.05 wt%, 0.1 wt% and 0.5 wt% by weight of cement, while the ratio of SWCNT/SDBS was kept constant at 1:1. Ultrasonication was performed for 60 min at 25% ($\sim 8 \text{ kJ}$) using the UP400S tip-ultrasonic probe processor (Hielscher Ultrasonics). Cementitious nanocomposites were prepared by mixing the SWCNT dispersions with cement at a water-to-cement ratio (w/c) of 0.5. The superplasticizer:SWCNT ratio was set to 10:1 allowing sufficient dispersion and appropriate workability. Generally, in cementitious nanocomposites, the filler content is given by the weight of the cement since the density of SWCNTs is mainly approximated due to their various amorphous contents. All cement composites were prepared with a standard mixing procedure using an IKA[®] EUROSTAR control 200 P4 equipped with an R 1381 propeller stirrer.

The SWCNT dispersions were introduced in a plastic container and the cement powder was introduced gradually during mixing at 320 rpm. After 5 min of total mixing time, a homogeneous slurry was obtained and casted in $10 \times 10 \times 60 \text{ mm}^3$ oiled steel moulds. The specimens were subsequently sealed in a plastic bag at 23–25 °C until testing. For electrical and thermoelectric measurements, the samples were measured at an age of 3, 7, 14 and 28 days. Hereinafter, the samples are denoted according to their nanofiller content, namely, the cement/SWCNT nanocomposite, which contains nanofillers at 0.5 wt% will be denoted as cement/SWCNT(0.5).

2.4 Characterization techniques

Raman spectra and maps were acquired using the 514.5 nm line of an argon ion laser operating at 1.0 mW at the focal plane. The HR-Horiba scientific system equipped with a 100 \times objective was used for the spectra acquisition, while a 50 \times long working distance (LWD) objective was used for mapping. A grating with 600 groves per mm was used, so that the wavenumber range from about 90 to 1800 cm^{-1} could be measured in a single window. To obtain accurate frequency

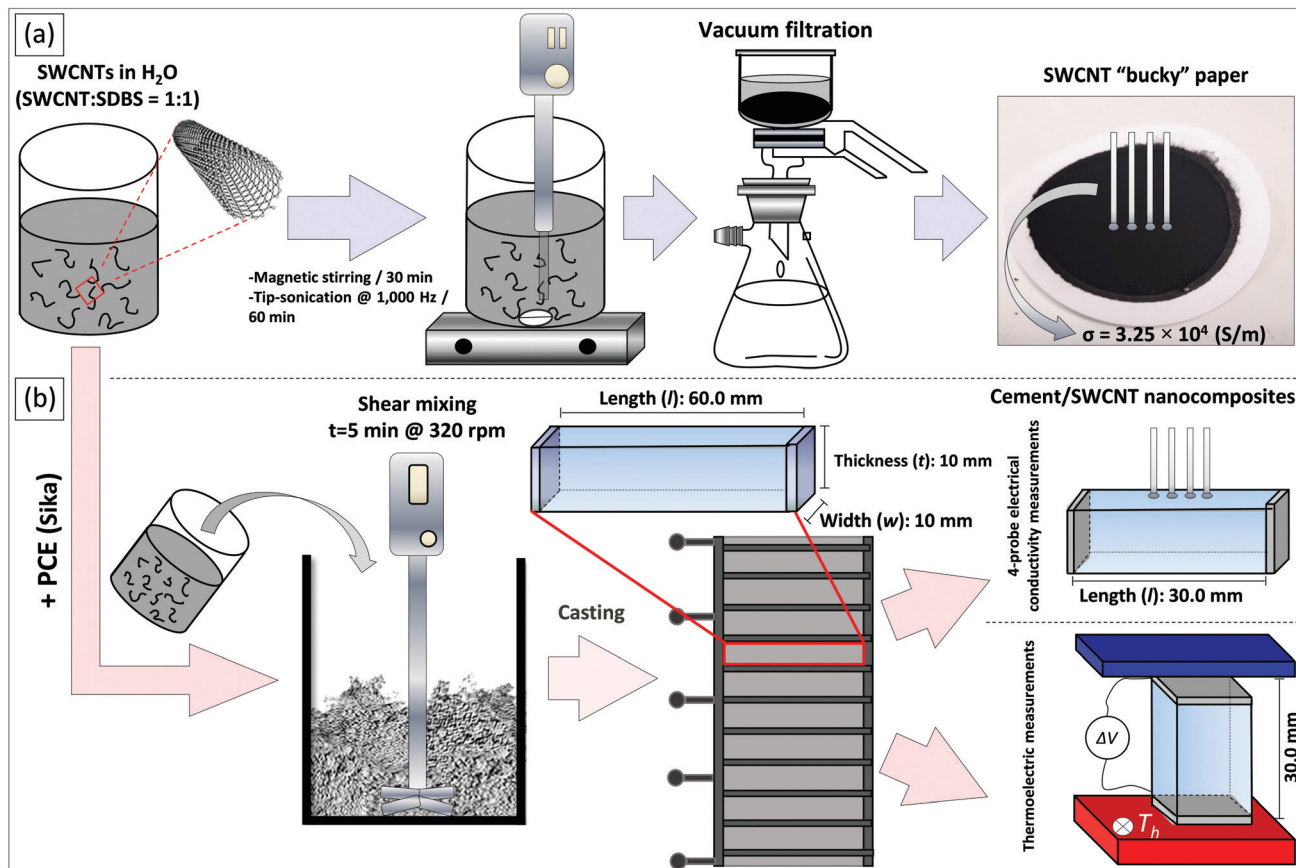


Fig. 1 Chemical schematic representation of the process towards (a) the preparation of a SWCNT bucky paper film (tip ultrasonication followed by a vacuum filtration process), and (b) the fabrication of cement/SWCNT nanocomposites *i.e.*, mechanical mixing of the p-type SWCNT dispersion, PCE and cement followed by casting resulting into $10 \times 10 \times 60 \text{ mm}^3$ samples (deposited Ag contacts at the ends of $10 \times 10 \times 30 \text{ mm}^3$ specimen were necessary for the Seebeck coefficient measurements).

position determination, spectral analysis, which involved the fitting of the known vibrational modes with Gaussian and Lorentzian distributions, was performed. For each specimen, mapping was carried out with the 'Swift mode' enabled, on an area of $30 \times 30 \mu\text{m}^2$ having a total of 256 points while the step size was $2 \mu\text{m}$. The number of points in the studied area is determined by the step size, which was selected to be higher than the size of the laser spot ($1.5 \mu\text{m}$). LabSpec6 software was used to control the instrument, refine the data and create Raman mapping images.

Scanning electron microscopy (SEM) was performed by means of an FEI NanoSem 200 (FEI, Eindhoven/The Netherlands) at an operational voltage of 5 kV. SEM was utilized to study the morphology of CNTs in the form of bucky paper as well as the morphology of cement/SWCNT nanocomposites.

A typical 4-probe technique using a commercial four-point probe system (Ossila Ltd) was employed for the calculation of the electrical conductivity (σ) of SWCNTs (in the form of bucky paper films) and the cement/SWCNT nanocomposites, based on the formula: $\sigma = \frac{1}{R_s} \times \frac{L}{S} \times \left(\frac{\ln 2}{\pi}\right)$, where R_s is the measured 4-probe sheet resistance, L is the length and S is the cross-section of each sample. For measuring the sheet resistance (R_s)

of the cement-based nanocomposites, the silver paste was deposited between the material's surface and the probes of the employed four-point probe system to improve their physico-chemical contact and increase the accuracy of the measurement. At least five measurements on different samples were performed to derive the mean values reported in this study.

The Seebeck coefficient of p-type SWCNTs (in the form of bucky paper films), as well as of the cement/SWCNT nanocomposites (specimen dimensions: $10 \times 10 \times 30 \text{ mm}^3$) was determined using a custom-made set-up. To enable the generation of a temperature gradient, all the samples were mounted on two metal blocks. For every measurement, one block was kept at room temperature (T_{cold} , at $25 \text{ }^\circ\text{C}$) while the other block (T_{hot}) was heated up *via* calibrated temperature-controlled resistors, allowing the generation of temperature difference (ΔT). For the thermoelectrically driven voltage measurement, Ag wires have been wrapped around the two end-point perimeters of the samples. The silver paste was also applied between the Ag wire and the sample surface to minimize the plausible contact resistance. The Ag wires were connected to an Agilent 34401A 61/2 digital multimeter to measure the generated thermovoltage (ΔV). An IR-thermometer (OMEGA OS-VIR50 Dual Laser Video IR Video Thermometer) was employed to measure the temperature

of the two blocks and determine the temperature difference (ΔT). The Seebeck coefficient (S) was derived then from the $\Delta V/\Delta T$ ratio.

Fig. 1 shows schematically the process towards the development of SWNT dispersions (Fig. 1a), and the mechanical mixing of the p-type SWCNT dispersion, PCE and cement towards the fabrication of $10 \times 10 \times 60 \text{ mm}^3$ cement/SWCNT nanocomposites (Fig. 1b). Samples of cement/SWCNT nanocomposites ($10 \times 10 \times 30 \text{ mm}^3$) with Ag contacts deposited at the ends of each specimen were used for the Seebeck coefficient measurements.

2.5 Fabrication and characterization of the cement/SWCNT based thermoelectric generator device

A cement/SWCNT based thermoelectric generator (TEG) was fabricated utilising the cement-based nanocomposite with the highest PF in this study, namely the cement/SWCNT(0.5) 28 day sample. More precisely, a device configuration of ten (10) thermoelements with a rectangular shape of $10 \times 10 \times 15 \text{ mm}^3$ electrically connected in series and thermally in parallel has been used.

For connecting each thermoelement, Ag conductive tape has been employed, connecting the cold side of each thermoelement with the hot side of the adjacent one. The conductive silver paste was also utilized between the Ag tape and the sample surface minimizing any contact resistance between the Ag electrodes with the TEG device thermoelements. The voltage output (V_{out} or open circuit voltage: V_{OC} or voltage of the TEG: V_{TEG}), internal resistance (R_{TEG}) of the device and short circuit current (I_{sc}) were measured with an Agilent 34401A 61/2 digital multimeter. The TEG device was placed on a hot plate with the “hot” surface of the device being exposed to $50 \text{ }^\circ\text{C}$ and $75 \text{ }^\circ\text{C}$, while the other surface (“cold”) was exposed to the environment ($25 \text{ }^\circ\text{C}$), resulting in a “through-thickness” temperature gradient of $\Delta T = 25 \text{ K}$ and $\Delta T = 50 \text{ K}$, respectively.

For the TEG device characterization, power measurements were performed for several different load resistances (R_{Load}) at the two different ΔT that the device was exposed to (25 and 50 K). Specifically, a homemade power output experimental set-up has been used in order to examine the TEG device power output characteristics as a function of different applied external load resistances (R_{Load}), described in detail in our previous work.³⁹ This set-up gives the open circuit voltage (V_{OC} or V_{TEG} , otherwise defined), and the short circuit current (I_{sc}), upon connecting the voltage meter and the Amp meter, respectively, as well as the V_{load} (V_L) and I_{load} (I_L) values for each of the different loads. For the power output measurements, various load resistances are applied and then the voltage and Amp meter are used to measure the voltage and current on the load resistance, allowing the calculation of the power output as $P_{\text{out}} = V_{\text{load}} \times I_{\text{load}}$ upon applying different external specific load resistances.

2.6 Finite element analysis (FEA) of cement/SWCNT based nanocomposite TEG device

Finite element numerical simulations have been developed and conducted, in order to investigate the thermoelectric behaviour of the proposed TEG device. It should be noted that the TEG device has been designed with the exact geometrical features of the actual experimental setup. ANSYS™ software was used for the

solution of the coupled constitutive equations governing thermoelectric phenomena with the appropriate boundary conditions.³⁹ The numerical solution provided thermal fields and electrical potentials, translated to temperature and voltage distributions throughout the device, as well as voltage differences between the input and output of the device. The mesh consisted of hexahedrons for the thermoelements and the Ag tape. To ensure a mesh-independent response, a convergence study was performed. Based on the convergence results determined for the thermoelectric response of the TEG device, a minimum element size of 1 mm was adequate to obtain acceptable accuracy in the calculated responses. Prior to the solution process, the necessary boundary conditions were introduced into the FEM solver. For each thermoelement, the “cold” surface was kept at room temperature, while the opposite surface was exposed to the temperature of the hot plate, following the experimental protocol. The heated surface of the first thermoelement had a voltage of 0 V (grounded), to direct the current flow of the electric energy generated by the temperature difference ΔT .

Two different FE models have been developed: a 10-thermoelement and a 100-thermoelement TEG module. The FE simulation results of the 10-thermoelement TEG module were compared with the measured data of the experimental setup to validate the accuracy of the numerical analysis. Then, a 100-thermoelement TEG module has been introduced to estimate the potential of the thermoelectric behaviour in an up-scaled device/module.

3. Results and discussion

3.1 Raman analysis of SWCNT powder and SWCNT bucky paper films and SWCNT microstructural characteristics

Raman spectroscopy is a powerful technique used to analyse the structural properties of materials, as many chemical substances have characteristic fingerprints in the Raman corresponding spectra. Fig. 2a shows the normalized Raman spectra of the as-received SWCNT powder (in black colour) and SWCNTs in the form of a bucky paper film (in red). All the commonly encountered features of SWCNTs are all present in both spectra. The vibrational modes that are present between 100 and 250 cm^{-1} are assigned to the radial-breathing modes of the resonantly excited nanotubes. The intensity of these peaks is enhanced in the spectrum of the bucky paper in comparison to the spectrum of the powder due to both the forms of the measured materials, thin planar form for the bucky paper and uneven thickness form for the powder, as well as due to the dispersion of the SWCNTs that caused the disentanglement of the tubes in the bucky paper sample, which is obvious in the spectrum by the increment in the intensity of the RBM peaks. The D mode (1303.6 cm^{-1} and 1334.8 cm^{-1}), a one phonon second order Raman scattering process that is usually attributed to the disorder, which is present in the material is also observed.⁴⁰

The intensity of the D band was increased, as expected, after the sonication process that was used for the dispersion of the SWCNTs and the preparation of the bucky paper. This increase is observed since a certain amount of shortening of the SWCNTs is

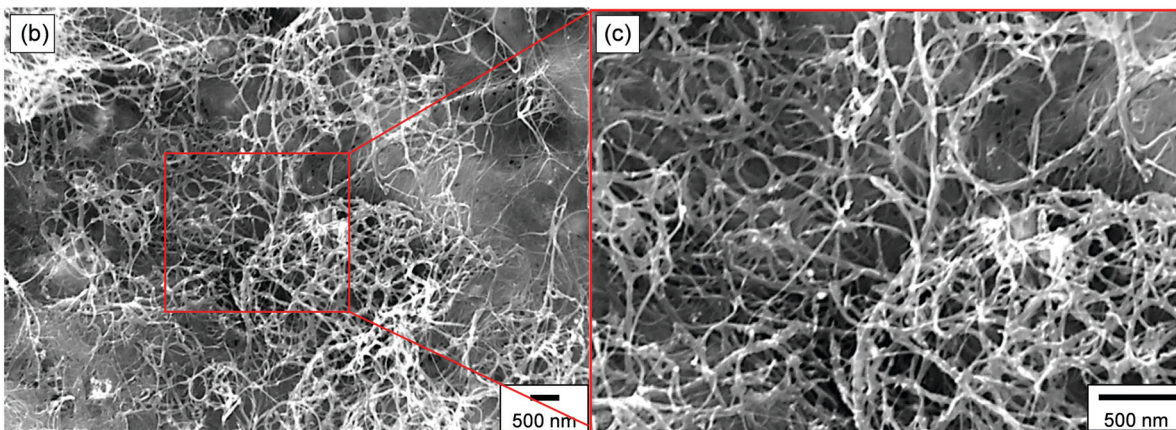
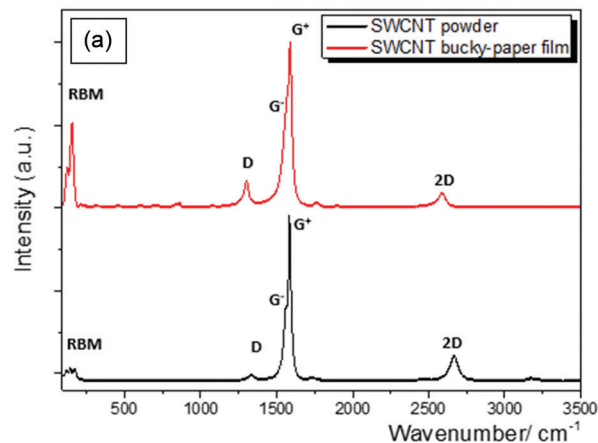


Fig. 2 (a) Raman spectra of the as received SWCNT powder, as well as of the bucky paper film (bucky paper prepared using the “freshly” produced SWCNT dispersion directly after the 60 min of tip sonication), (b) and (c) SEM images of SWCNTs in the form of a bucky paper film, at two different magnifications.

always caused by the sonication process⁴¹ leading to the inclusion of more SWCNT edges in the acquired spectrum.⁴² The double vibrational mode, which was observed at about 1590 cm⁻¹ is the G-band, a Raman-signature peak for SWCNTs. This band is comprised of two components, the G⁺ peak at 1584.1 cm⁻¹ and the G⁻ peak at 1564.1 cm⁻¹ in the spectrum of the SWCNTs in powder form. The position of the G⁺ and G⁻ peaks appeared to be blue-shifted to 1588.3 cm⁻¹ and 1568.4 cm⁻¹, respectively, in the bucky paper's spectrum. Furthermore, the line shape of the G⁻ band showed that the SWCNTs are semiconductors (Lorentzian line shape).⁴³

Highly disentangled SWCNTs studied in the form of bucky papers can be observed by the SEM analysis (see Fig. 2b and c). High aspect ratio SWCNTs corroborate the data sheet of OCSiAl Tuball (aspect ratio = 166, length > 5 μm, diameter = 1–3 nm). The high length of SWCNTs reveals that the sonication optimum process has not significantly affected their lengths, so that percolation at low weight percentages could be realized in the cementitious nanocomposites. Some spherical bright particles that are observed can be identified as metallic catalysts from the synthesis.

3.2 Electrical conductivity of cement/SWCNT nanocomposites

The electrical conductivity of the cement/SWCNT nanocomposites at 3, 7, 14 and 28 days along with the corresponding

standard deviation is shown in Fig. 3a. In conductive cement nanocomposites with carbon-based nanofillers, electrons (electronics charge carriers), as well as ions (ionic charge carriers) contribute to the experimentally measured electrical conductivity in a mixed electrical transport carrier transport mechanism. With a high water content at the first days of hydration (3 d and 7 d), ionic conductivity is dominant, whereas as the hydration of cement proceeds and C–S–H gel is formed, free pore water decreases, and the electrical conductivity is promoted due to electronic charge carriers' contribution. Additionally, cementitious crystals nucleate and repel the SWCNTs to the boundaries developing an enhanced SWCNT network (otherwise known as the “volume exclusion effect”). As such, a denser SWCNT conductive network enables enhanced charge-carrier transport, together with the sample's moisture that is eliminated during the cement hardening process.

The higher electrical conductivity ($\sigma = 1.59 \times 10^3 \text{ S m}^{-1}$) corresponds to the higher SWCNT loading, since the SWCNT–SWCNT distance reduces, and a higher filler concentration produces a better condition for networking, extended CNT–CNT junctions, and shorter conductive pathways.

As seen in Fig. 3b, already even from a very low SWCNT content, (0.005 wt%), the cement/SWCNT nanocomposites are above their electrical percolation threshold with a conductivity

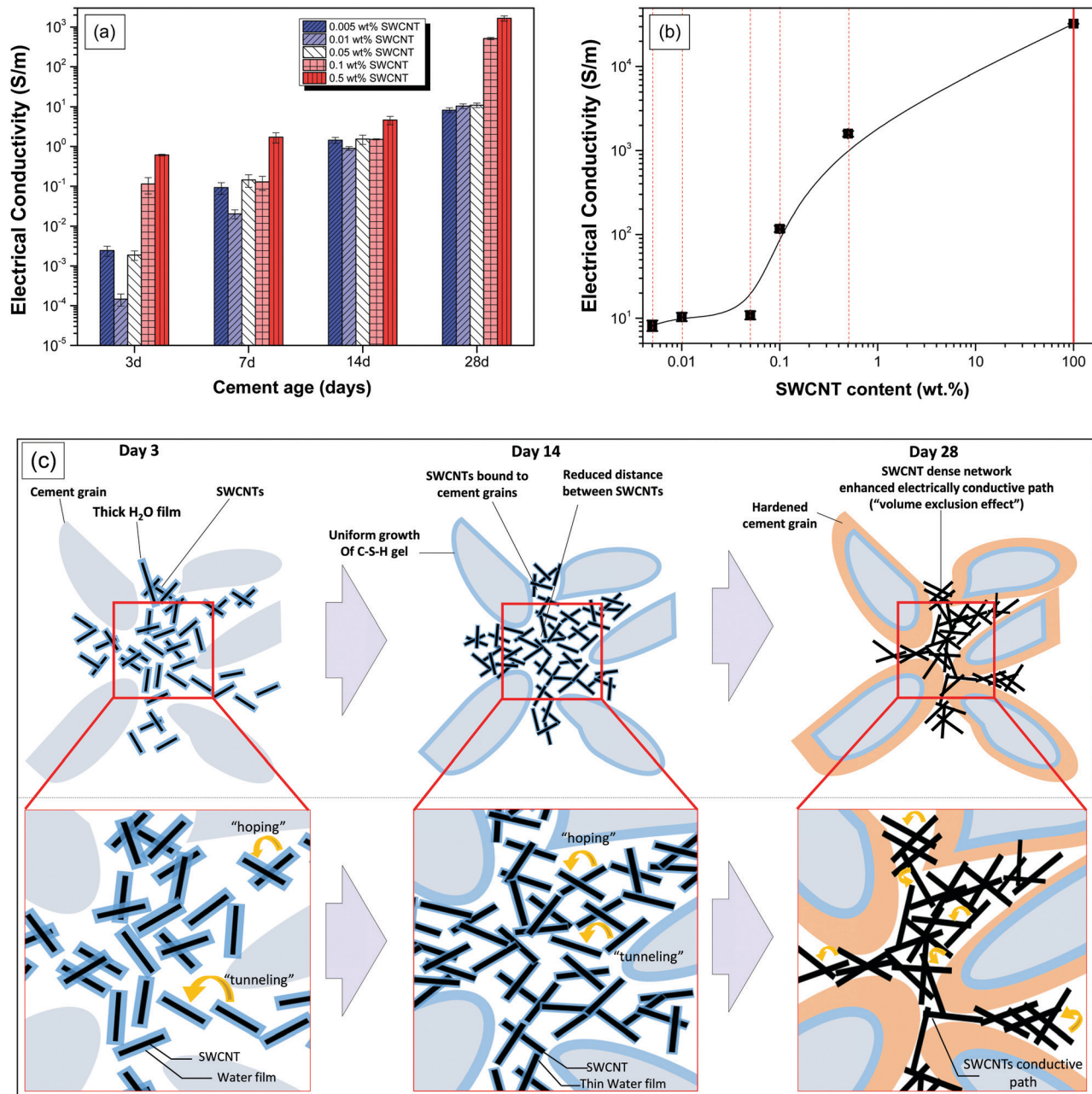


Fig. 3 (a) Electrical conductivity (σ in S m^{-1}) for cement/SWCNT nanocomposites at 0.005 wt%, 0.01 wt%, 0.05 wt%, 0.1 wt%, and 0.5 wt% at different ages (3 d, 7 d, 14 d and 28 d), and (b) Conductivity curve evolution for the cement/SWCNT nanocomposites at the age of 28 days. (c) Schematic illustration of the SWCNT conductive network development into the cementitious matrix during cement hydration (days 3, 14, and 28), and the striking charge-carrier mechanisms over time with an occurring "volume exclusion effect".

value ranging from 0.8 to 0.9 S m^{-1} . The conductivity remains almost the same up to 0.05 wt% SWCNT filler loading and only slightly increases reaching $\sim 1.0 \text{ S m}^{-1}$. By increasing further the SWCNT content, namely, at 0.1 wt%, the SWCNT conductive network probably consists of much shorter carrier transport paths, resulting in an enormous conductivity increase of approx. two orders of magnitude ($\sigma = 117 \text{ S m}^{-1}$). For the 0.5 wt% SWCNT content, the conductivity increases even further by an order of magnitude slightly above 10^3 S m^{-1} , which is an extremely high value for such a low amount of conductive

nanofillers considering that the SWCNT inherent electrical conductivity was $3.25 \times 10^4 \text{ S m}^{-1}$ (represented by the continuous red line in Fig. 3b) measured in the form of a bucky paper film.

For the proper evaluation of the electrical conductivity of cement/SWCNT nanocomposites, we need to consider the discrete phenomena taking place throughout cement hydration along with the SWCNT charge-carrier transport mechanisms. Fresh cement paste (a reactive particle suspension) is formed when cement powder is mixed with water. The properties of the cement paste develop over time, as the hydration products,

mainly calcium–silicate–hydrate (C–S–H), are formed. Nano-scale C–S–H grow onto the micron sized clinker grains sticking them together.⁴⁴ The addition of SWCNTs to cement pastes influences the formation and structure of the C–S–H and other products formed during hydration. Initially, most of the SWCNTs are dispersed in the pore water of the cementitious matrix, having limited interconnections resulting in a relatively low electrical conductivity. As the hydration of cement proceeds over time, C–S–H and crystals, such as ettringite or portlandite, grow further and a part of the SWCNTs get repelled to the boundaries of these crystals, developing percolated SWCNTs networks, similar to segregation or otherwise defined as a “volume exclusion effect” that has been reported for polymer blend systems.⁴⁵ Larger hydration products result thereby in a more effective volume exclusion effect. In addition, since the distance between the adjacent SWCNTs is decreasing, this gives rise to the formation of improved conductive paths and charge-carrier transport *via* a plausible ‘hopping’ or ‘tunneling’ mechanism (Fig. 3c).

3.3 Raman mapping of cement/SWCNT nanocomposites

In Fig. 4, the normalized Raman spectra of a pristine cement specimen (in black colour), a cement/SWCNT(0.005) nanocomposite (in red colour) and a cement/SWCNT(0.5) nanocomposite (in blue colour) are depicted. In the pristine cement specimen, CaCO_3 polymorphs (calcite, aragonite, vaterite) due to relative translations between anionic and cationic groups of the pristine cement can be observed at 161 cm^{-1} , 240 cm^{-1} and 1088.5 cm^{-1} such as lattice-type vibrations of the carbonate group, Ca-O polyhedra and the ν_1 vibration mode corresponding to the case where every CO_3 group vibrates in identical phases.⁴⁶ Peaks at 768.2 cm^{-1} and 789.5 cm^{-1} are attributed to the unreacted clinker phases tricalcium silicate or alite (C_3S) and dicalcium silicate or belite (C_2S).⁴⁷ Finally, the peak at 967.7 cm^{-1} is assigned to the $\nu_1(\text{SiO}_4)$ Si–O symmetrical stretching indicating the presence of ettringite crystals, which were also discerned from the SEM analysis.⁴⁶

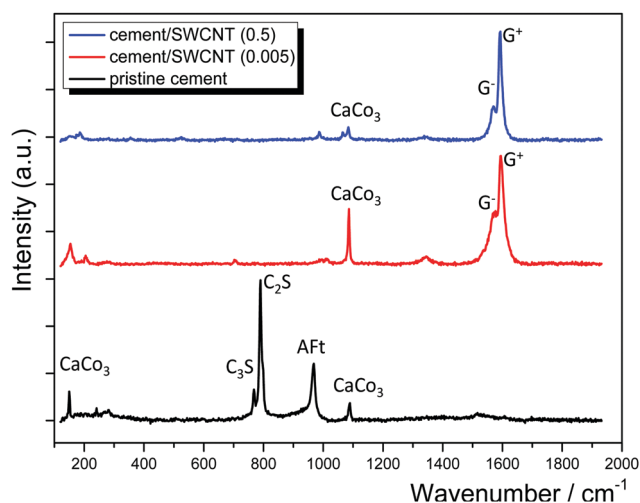


Fig. 4 Raman spectra of a pristine cement specimen (black colour), cement/SWCNT(0.005) (red colour) and cement/SWCNT(0.5) (blue colour) nanocomposites.

In the SWCNT-based cement nanocomposites, the interactions between the SWCNTs and the cementitious matrix can be identified as intensity changes, and/or bandwidth changes in the Raman peaks of SWCNTs.⁴³ A shift in the position of the G band of SWCNTs is generally caused by the interactions between SWCNTs and the cementitious matrix *via* non-covalent surface modification, or adsorption of the hydrophobic part of the surfactant at nanotubes sidewalls through van der Waals, π – π or CH– π . The spectrum of the cement/SWCNT nanocomposites (Fig. 4) shows blue-shifts of the D,G peaks in comparison to the spectrum of the SWCNT bucky paper (Fig. 2a) and the spectrum of the pristine cement (Fig. 4). The blue-shifts can arise from the charge transfer between SWCNTs and the matrix or from changes in the SWCNT–SWCNT interactions due to their dispersion in the cementitious matrix.

Moreover, as we have already seen in detail the volume of the SWCNTs influences the crystallization process of the cement, giving rise to different micro-phases in the structure of the cementitious matrix, which explains the differences in the Raman spectra of the cement/SWCNT nanocomposites. To clarify the effect of nanodispersions and its spatial distribution inside the cementitious matrix, Raman images were collected during continuous x – y stage movement (SWIFT© mode). Generally, exceptional spectral quality can be achieved if a point-by-point mapping approach is employed, as it is enhanced from longer acquisition times. Nevertheless, in the work at hand Raman images were recorded with the SWIFT© mode for reasons of saving imaging time and maximizing the imaging area. It should be noted that even poor-quality spectra contain sufficient details for peaks, including for the identification of the phases.

Fig. 5 shows the surface Raman images for the cement/SWCNT(0.005) (a and b) and cement/SWCNT(0.5) nanocomposites (c and d), respectively. At the centre of the images, indicative spectra acquired with the SWIFT© mode are depicted and the peaks of interest (G^+ band for the SWCNT, and characteristic CaCO_3 peak for the cement nanocomposites) are highlighted.

At the sides, baseline-corrected intensities of the marked bands result in the presented phase distribution maps. The maps on the left side illustrate the distribution of the graphitic, G^+ peak, while those on the red side represent the G^+/CaCO_3 ratio. The vibrational mode of CaCO_3 was selected as the denominator of the fraction as we intend to examine the distribution of the SWCNTs in the cementitious matrix. Dark blue colours correspond to the highest intensities of the G^+ peak in the maps of Fig. 5a and c, while the lowest intensities are shown in red colour. The same colour scale was also used for the G^+/CaCO_3 intensity ratio maps in Fig. 5b and d. It can be clearly observed in Fig. 5a and c, that SWCNTs were homogeneously dispersed throughout the cementitious matrix in both the low and the high SWCNT nanocomposite loadings. The G^+/CaCO_3 intensity ratio is low (0–15) in the majority of the cement/SWCNT(0.005) map, while in a few spots the intensity is up to 15–35. In contrast, in the high-volume nanocomposite (cement/SWCNT(0.5) map), more sites with high (15–40) G^+/CaCO_3 intensity ratios are evident.

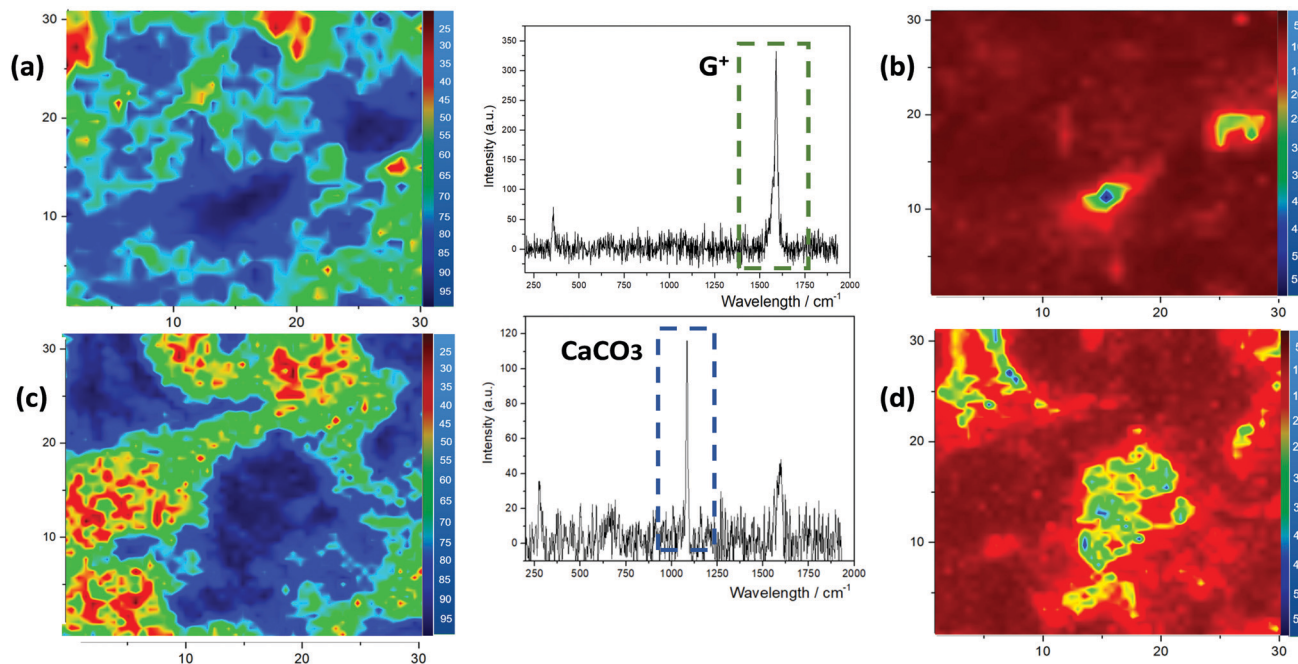


Fig. 5 Raman intensity maps (area of $30 \times 30 \mu\text{m}^2$) of (a and b) cement/SWCNT(0.005) and (c and d) cement/SWCNT(0.5) nanocomposites revealing the distribution of the SWCNTs inside the cementitious matrix.

3.4 SEM microstructural analysis of cement/SWCNT nanocomposites

The microstructure of the cement/SWCNT (0.5) nanocomposite at an age of 28 days is shown in Fig. 6. Finely dispersed SWCNTs, building a percolated network, can be observed distributed within the cementitious matrix, verifying the high electrical conductivity. Moreover, the nanofillers contribute to the bridging of cement grains, possibly also cracks bridging at the nanoscale. Along the SWCNT lengths, hydrated phases in the form of ettringite and C-S-H were found. These were also identified *via* the Raman analysis above.

3.5 Thermoelectric properties of cement/SWCNT nanocomposites

The Seebeck coefficients reported in this study are those at a steady state, after 5 minutes of exposing the cementitious nanocomposites to a thermal difference (ΔT). As shown in Fig. 7, a decay in time is observed at the open circuit potential of the thermoelement (V_{TE} or V_{OC}), thus at the Seebeck coefficient. The Seebeck coefficient in cement nanocomposites enhanced with SWCNT, originates from a superposition of the thermo-diffusion of electronic charge carriers (holes and electrons) and the diffusion of ions (anions and cations), $S = S_{\text{el}} + S_{\text{ionic}}$. Holes, in our case,

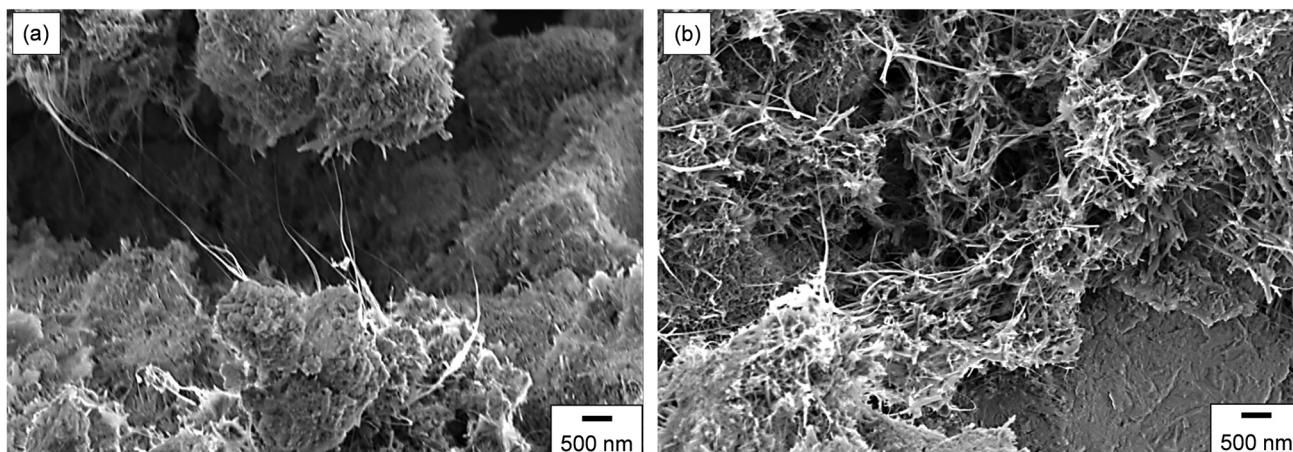


Fig. 6 (a and b) SEM images of the cement/SWCNT(0.5) nanocomposite at the fractured surface at the age of 28 days, at two different positions showing cement phases, as well as homogeneous dispersed and disentangled SWCNTs in the cement matrix.

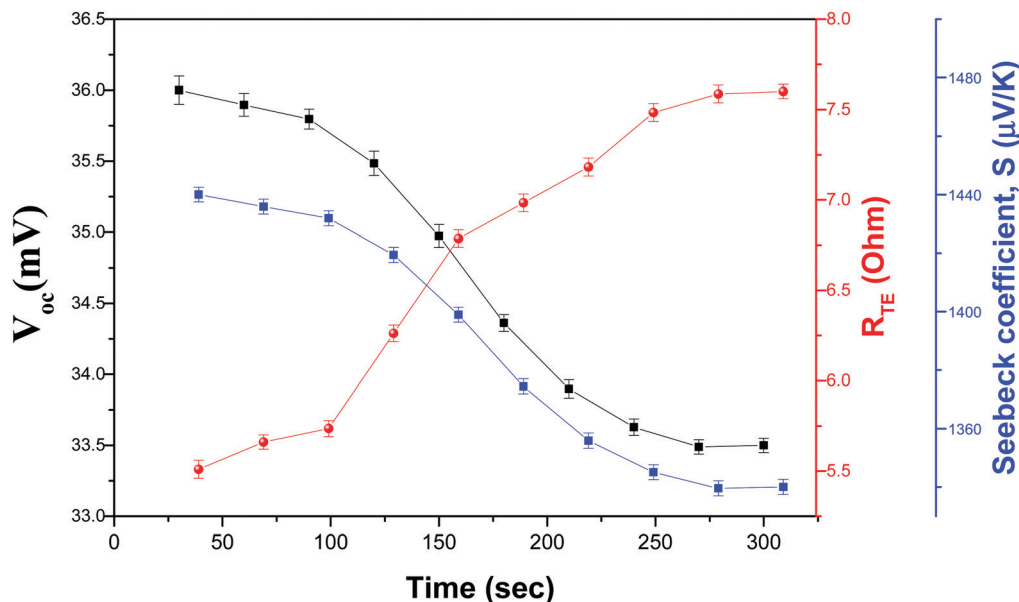


Fig. 7 Thermoelectric properties over time for the 28 day cement/SWCNT(0.5) sample.

reach the contacts and are capable of further surpassing the contact to an external circuit. On the other hand, ions tend to accumulate towards the contacts. The Soret effect prompts a selective ion attachment to the respective metallic electrode, anode or cathode and conducts the creation of an electric potential difference between the cold and the hot side, and in other words, the ionic Seebeck coefficient. Electrochemically active or redox molecules are not present in our case, thus thermogalvanic effects are excluded.⁴⁸

Therefore, the potential is high due to both the holes and the ions. However, ions accumulated at the metal electrodes induce a decrease over time, a decay when the ions are consumed similar to a thermoelectric battery.⁴⁹ The S value obtained for cement/SWCNT(0.5), which also presented the higher measured electrical conductivity, was $1348.8 \mu\text{V K}^{-1}$ at $\Delta T = 25 \text{ K}$, the highest reported with respect to the low SWCNT content.¹² We intentionally chose a relatively low thermal gradient, since the potential of this cement-based TE technology is to be implemented in buildings or pavements where extreme thermal gradients are most of the time uncommon.

Fig. 8a and b present the absolute Seebeck coefficient (S) and the calculated PF together with the corresponding standard deviation values for the cement/SWCNT nanocomposites at an age of 3, 7, 14 and 28 days. The positive sign of the S indicates that the cement nanocomposites are, in analogy to solid state semiconductors, p-type semiconductors, meaning the cations thermally diffuse easier than the anions along with the prevalence of holes over electrons as the major electronic charge carriers. The lower SWCNT content contributes to larger Seebeck coefficients. These enhanced S values are due to the adsorbed water by the SWCNTs and the cement structure allowing the thermal diffusion of ions contributing to the overall thermopower. When below the percolation threshold, the Seebeck coefficient increases significantly over time whereas at the

threshold and above of it, it decreases (all values are summarised in Table 1).

3.6 Cement/SWCNT TEG device performance and power output characteristics

Fig. 9a illustrates schematically the equivalent circuit of the cement/SWCNT based TEG device. All details regarding the device fabrication have been described in the experimental part of this study. Fig. 9b depicts the real TEG with the corresponding dimensions, utilising the cement/SWCNT(0.5) p-type nanocomposite with the highest achieved power factor ($2.89 \times 10^3 \mu\text{W m}^{-1} \text{K}^{-2}$). As it can be observed, the device consists of ten (10) thermoelements serially interconnected. Ag conductive tape was used as the metallic junction for the thermoelement interconnection and the TEG device realization. Fig. 9c shows the infrared thermography (IR-T) image of the TEG device upon being exposed to a temperature gradient of $\Delta T = 25 \text{ K}$.

Fig. 9d–f show the digital photographs of the TEG device under test at $\Delta T = 25 \text{ K}$ (hot side: $50 \text{ }^\circ\text{C}$; cold side: room temperature $25 \text{ }^\circ\text{C}$) showing the experimentally measured R_{TEG} , V_{TEG} (otherwise defined as V_{out} or open circuit voltage V_{OC} of the device) and short circuit current (I_{sc}), respectively. As it can be seen, the TEG device generates a V_{TEG} of 15.7 mV with an I_{sc} of 0.429 mA at an internal device resistance $R_{TEG} = 48.8 \Omega$. It is worth mentioning that the expected and theoretical V_{TEG} would be 337 mV considering the formula $N \times S \times \Delta T$.

However, the experimentally measured V_{TEG} value has been 15.5 mV , revealing that each thermoelement in the serial interconnection contributed by 1.55 mV to the total V_{out} of the device ($V_{TEG} = V_1 + V_2 + V_3 + \dots + V_{10}$). This in other words could indirectly yield a new Seebeck coefficient value for the cement/SWCNT(0.5) active thermoelement material, which practically is not the measured one at the thermoelement level

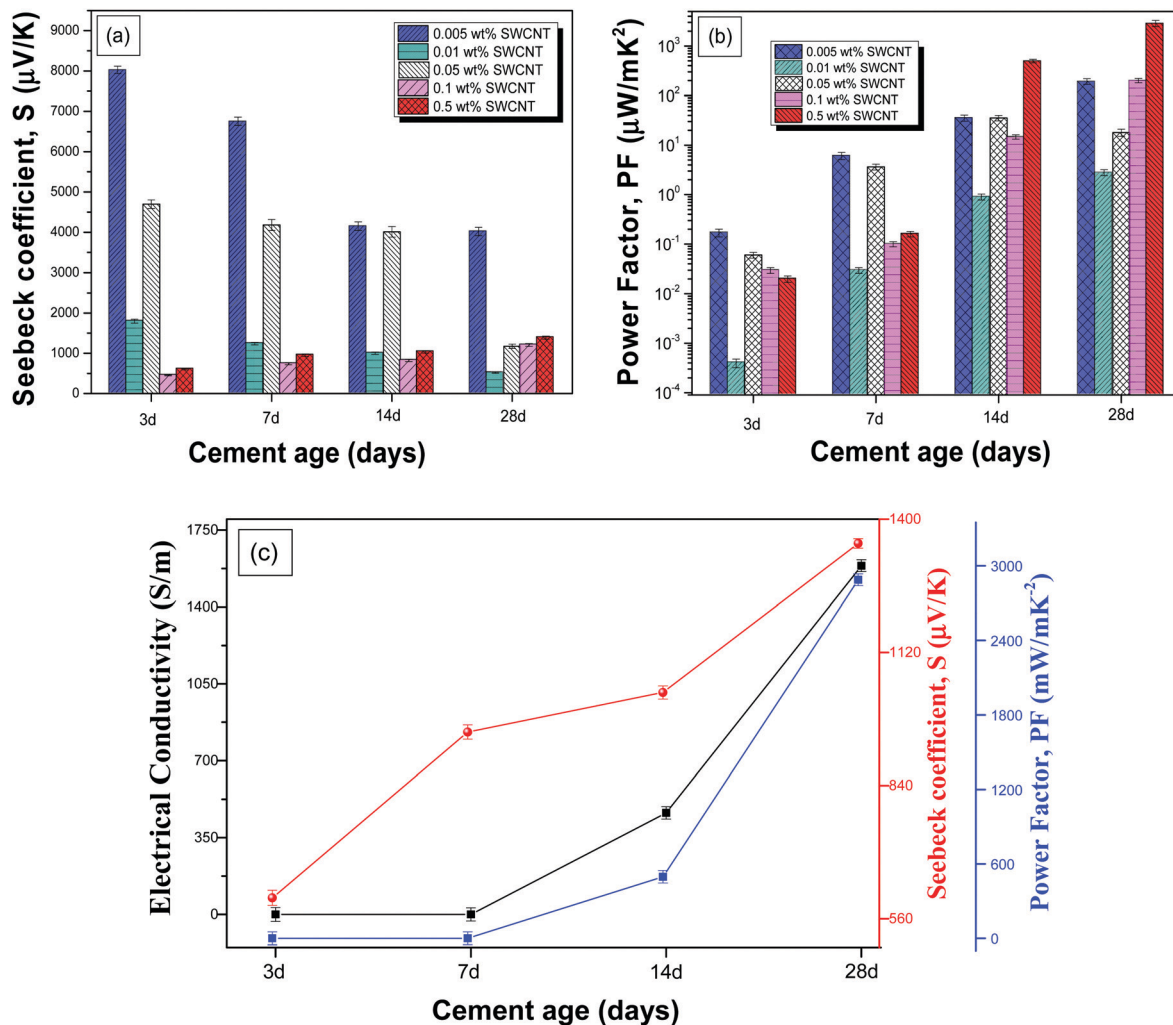


Fig. 8 Thermoelectric properties: (a) S and (b) PF of cement/SWCNT nanocomposites with 0.005 wt%, 0.01 wt%, 0.05 wt%, 0.1 wt%, and 0.5 wt% nanofiller loading at different ages (3 d, 7 d, 14 d and 28 d). (c) The σ , S , and PF values of the cement/SWCNT(0.5) nanocomposite at different ages (3 d, 7 d, 14 d and 28 d).

and as plotted in Fig. 8a. Specifically, following the formula $S = \Delta V/\Delta T$ and considering 1.55 mV produced by each thermoelement at $\Delta T = 25$ K, the Seebeck coefficient is calculated to be approx. $62.8 \mu\text{V K}^{-1}$. This is a very interesting finding since the Seebeck coefficient of the p-type SWCNTs used in this study and measured in the form of a bucky paper film was $33.2 \mu\text{V K}^{-1}$. It could be speculated that the cement ions are not being harvested to the external circuit at the TEG device level; however, they probably contribute to some kind of charge-transfer doping to the SWCNTs enhancing their p-type character as similarly found in another study.³⁸ As is already known, migration rates of ions are very slow as they tend to stay motionless and even though they cannot pass into the metallic electrodes, they provide the thermovoltage necessary to induce a quasi-constant power output thanks to the charge carriers. In conclusion, p-type cement/SWCNT nanocomposites act differently when incorporated into a TEG device. The decreased V_{out} of the TEG device compared to the expected and theoretical one affects also the maximum electrical power output (P_{max}) of the

cement-based TEG device, which is known to be calculated by the following equation (eqn (2)):⁵⁰

$$P_{\text{max}} = \frac{(NS\Delta T)^2}{4R_0} = \frac{\Delta V^2}{4R_0} \quad (2)$$

where N is the number of p-type cement/SWCNT(0.5) thermocouples, S is the Seebeck coefficient, and ΔT is the temperature difference. Quantity P_{max} is the maximum output of electrical power and R_0 is the internal electrical resistance of the TE generator (otherwise stated as R_{TEG}).

Namely, the expected P_{max} considering the experimentally measured Seebeck coefficient at the thermoelement level [$S = +1348.8 \mu\text{V K}^{-1}$ for the cement/SWCNT(0.5) shown in Fig. 10a] would be $579.4 \mu\text{W}$ at $\Delta T = 25$ K. However, the P_{max} of the device considering the experimentally measured V_{TEG} at $\Delta T = 25$ K and the second part of Eqn 2 is calculated to be $1.26 \mu\text{W}$.

As we have partly discussed, under a thermal gradient and due to the Soret effect, ions are accumulated in the contacts,

Table 1 Electrical conductivity (σ), Seebeck coefficient (S) and power factor (PF) values for the different p-type cement/SWCNT nanocomposites

Investigated material	σ (S m ⁻¹)	S ($\mu\text{V K}^{-1}$)	PF ($\mu\text{W m}^{-1} \text{K}^{-2}$)
SWCNT (bucky paper film)	$3.25 \times 10^4 \pm 10.45$	33.2 ± 1.10	35.45
Cement/SWCNT(0.005)_3d	$2.45 \times 10^{-3} \pm 0.01$	8023 ± 108.26	0.17
Cement/SWCNT(0.005)_7d	$9.23 \times 10^{-2} \pm 0.08$	8106 ± 106.24	6.10
Cement/SWCNT(0.005)_14d	$1.44 \times 10^0 \pm 0.12$	4976 ± 97.42	35.60
Cement/SWCNT(0.005)_28d	$8.20 \times 10^0 \pm 1.18$	4822 ± 96.24	191.85
Cement/SWCNT(0.01)_3d	$1.47 \times 10^{-4} \pm 0.01$	1800 ± 49.57	0.0004
Cement/SWCNT(0.01)_7d	$2.04 \times 10^{-2} \pm 0.07$	1240 ± 34.11	0.03
Cement/SWCNT(0.01)_14d	$8.96 \times 10^{-1} \pm 0.65$	1000 ± 27.50	0.90
Cement/SWCNT(0.01)_28d	$1.04 \times 10^1 \pm 1.21$	516 ± 13.40	2.80
Cement/SWCNT(0.05)_3d	$1.88 \times 10^{-3} \pm 0.01$	5632 ± 104.82	0.06
Cement/SWCNT(0.05)_7d	$1.44 \times 10^{-1} \pm 0.15$	5016 ± 102.50	3.65
Cement/SWCNT(0.05)_14d	$1.53 \times 10^0 \pm 0.14$	4812 ± 95.90	35.50
Cement/SWCNT(0.05)_28d	$1.09 \times 10^1 \pm 1.22$	1290 ± 35.80	18.10
Cement/SWCNT(0.1)_3d	$1.14 \times 10^{-1} \pm 0.18$	540 ± 14.50	0.03
Cement/SWCNT(0.1)_7d	$1.28 \times 10^{-1} \pm 0.21$	886 ± 25.34	0.10
Cement/SWCNT(0.1)_14d	$1.51 \times 10^1 \pm 1.45$	988 ± 27.41	14.75
Cement/SWCNT(0.1)_28d	$1.17 \times 10^2 \pm 10.1$	1312 ± 35.82	201.30
Cement/SWCNT(0.5)_3d	$6.09 \times 10^{-2} \pm 0.06$	604 ± 16.63	0.02
Cement/SWCNT(0.5)_7d	$1.72 \times 10^{-1} \pm 0.65$	952 ± 26.82	0.16
Cement/SWCNT(0.5)_14d	$4.63 \times 10^2 \pm 40.50$	1035 ± 28.41	496.50
Cement/SWCNT(0.5)_28d	$1.59 \times 10^3 \pm 120.10$	1348 ± 37.08	2887.70

and they cannot flow towards the adjacent thermoelements of the device. As a result, they are consumed in a closed circuit, and are unable to pass to the external circuit in which the voltage (V_{OC}) and current (I_{sc}) are measured, as similarly reported elsewhere.^{49,51} Lacking electrochemical reaction at the electrodes, ions cannot pass through the contacts to an external circuit and incite a continuous current; therefore, the V_{out} at the TEG device terminal is much smaller than the expected and basically only due to the thermoelectrically generated electronic charge carriers.⁵²

Practical use of the TEG devices requires power generation, which has been measured in our study using a homemade apparatus. Specifically, power measurements on the cementitious TEG device were performed for several different load resistances (R_{load}), at the two different values of ΔT that the device was exposed to (25 and 50 K). Specifically, Fig. 9a shows the equivalent circuit model of the TEG device, where the power measurements have been carried out. Fig. 9g shows the experimental output voltage-current ($V-I$) and output power-current ($P-I$) curves, while 9 h the $V-R_L$ and $P-R_L$ curves at two different ΔT (25 and 50 K), applying different external load resistances (R_L ; R_{load}). The continuous lines in all curves have been derived from calculations of the following formula (eqn (3)), giving the output power (P):

$$P = I^2 R_{load} = \left(\frac{V_{OC}}{R_{in} + R_{load}} \right)^2 R_{load} \quad (3)$$

where I is the output current (defined also as I_L ; current which passes through the load), R_{load} or R_L is the load resistance, R_{in} is the internal resistance of the device (otherwise defined as R_{TEG}) and V_{OC} is the open circuit voltage (equal to the measured V_{TEG}) when the R_{load} approaches infinity.

It can be observed that the output voltage for the different R_{load} applied is inversely proportional to the output current. Moreover, the maximum power generation of 5.02 μW at

$\Delta T = 50$ K and 1.28 μW at $\Delta T = 25$ K (Fig. 9h), respectively, could be observed when R_{load} matches with the internal TEG resistance. The P_{max} , otherwise known as the maximum electric power, dissipated in the load resistor, is realised when the load resistance is equal to the TEG device resistance (R_{TEG}). Moreover, at a load resistance of 49 Ω (Fig. 9h), the thermoelectric power voltage V_{TEP} was 7.9 mV, compared to an open circuit voltage (V_{OC}) of 15.7 mV at $\Delta T = 25$ K, while V_{TEP} was 15.2 mV, compared to a V_{OC} of 30.05 mV at $\Delta T = 50$ K. Above 49 Ω , V_{TEP} continues to increase as it approaches the open circuit voltage (V_{TEG}), but P decreases as the load resistance increases. The squared behaviour of V_{TEP} was expected due to the relationship $P = V_L^2/R_L$.

The thermoelectric performance of the TEG device was also studied by finite element analysis (FEA). The examined TEG device was modelled in correspondence with the experimental setup, adopting the reported thermoelectrical properties of the cementitious thermoelements *i.e.*, $S = 62.8 \mu\text{V K}^{-1}$. The coupled differential equations describing the thermoelectric effect allowed the detailed simulation of the performance of the proposed cementitious TEG device, exposed to different temperature gradients. In the FE model, the imposed temperatures of the hot plate (50 °C and 75 °C), as well as the room temperature (25 °C), were applied to the bottom and the top surface of each thermoelement, respectively, as portrayed in Fig. 9a.

In Fig. 10a, the temperature distribution through the thermoelements in the case of $\Delta T = 25$ K is depicted. It should be mentioned that identical temperature distribution is demonstrated among all the thermoelements. The serial interconnection of the thermoelements has been confirmed by the electric potential distribution, as illustrated in Fig. 10b, where the produced output voltage can be calculated from the summation of each thermoelement voltage. The device generates a V_{TEG} of 15.35 mV and 30.7 mV at $\Delta T = 25$ K and 50 K, respectively.

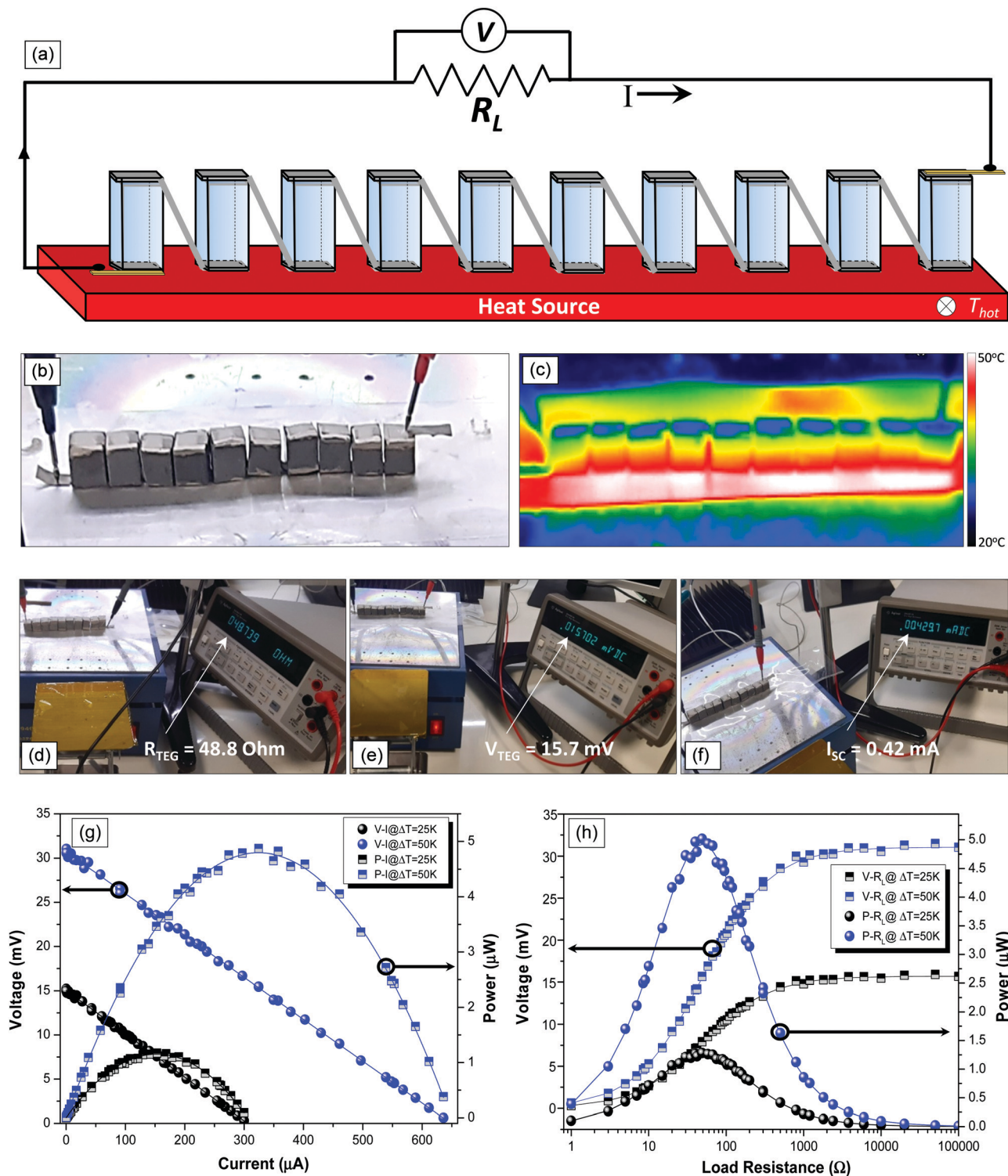


Fig. 9 (a) Schematic illustration of the TEG module equivalent circuit consisting of 10 p-type cement/SWCNT(0.5) nanocomposite blocks electrically connected in series, (b) the real TEG device upon being exposed to $\Delta T = 25$ K and (c) the corresponding IR-T image showing thermal distribution, (d–f) the digital photographs of the TEG device under test at $\Delta T = 25$ K showing the device electrical characteristics *i.e.*, R_{TEG} , V_{OC} , and I_{sc} . (g) The experimental output voltage–current ($V-I$) and output power–current ($P-I$) curves, and (h) the $V-R_L$ and $P-R_L$ curves (g and h plots correspond to the measurements upon the exposure of the device to two different ΔT *i.e.*, 25 and 50 K, applying different external load resistances R_L). The peak power at $\Delta T = 25$ K and $\Delta T = 50$ K occurred when the R_{Load} matches the internal TEG resistance.

These numerical values are in good agreement with the experimental measurements. Thereby, room temperature (25 °C) was

applied to the bottom and the top surface of each thermoelement, respectively, as portrayed in Fig. 9a.

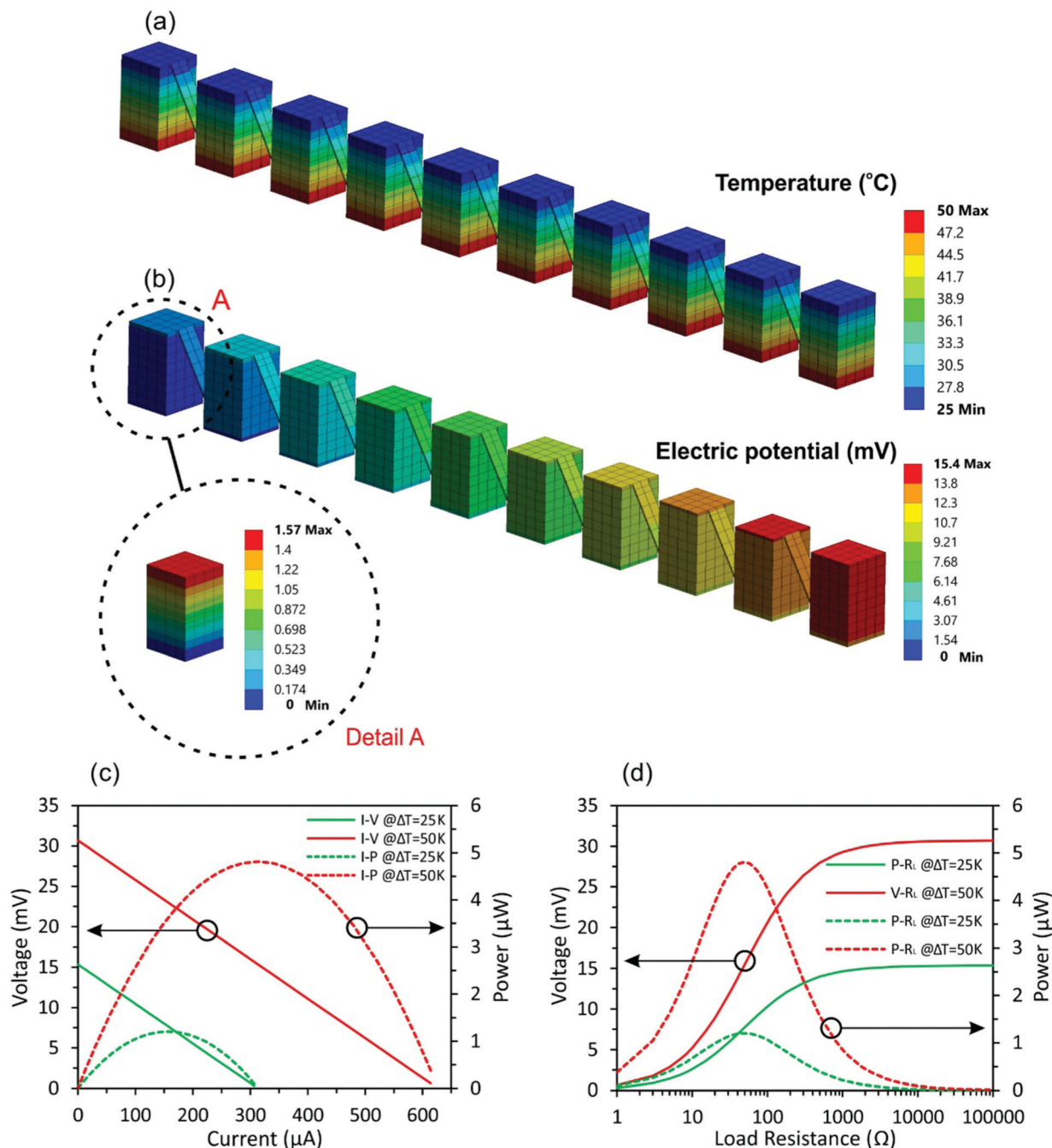


Fig. 10 (a) Temperature and (b) electric potential distribution through the TEG device exposed to $\Delta T = 25$ K. (c) $V-I$ and $P-I$ curves, and (d) $V-R_L$ and $P-R_L$ curves.

The device generates a V_{TEG} of 15.35 mV and 30.7 mV at $\Delta T = 25$ K and 50 K, respectively. These numerical values are in good agreement with the experimental measurements. Thereby, it is concluded that the proposed FE method has shown to be a very effective approach to characterize the thermoelectric behaviour of the proposed cementitious TEG device. Given the experimentally measured internal device resistance (R_{TEG}), $V-I$ and $P-I$ data (Fig. 10c), as well as $V-R_L$ and $P-R_L$ data (Fig. 10d) were calculated by Eqn (3) for the two different gradients.

Moreover, the P_{max} values were evaluated to be 1.2 μW and 4.81 μW at $\Delta T = 25$ K and 50 K, respectively. The computationally

generated maximum power density of the cementitious TEG device has been calculated to be 4.81 mW m^{-2} at $\Delta T = 50$ K.

A TEG device consisting of 100 serially interconnected thermoelements was also simulated to evaluate the electric potential of a higher scale generator. The material properties and thermal exposure imported in the FEM were the same as described in the previous simulation. In Fig. 11a the TEG assembly is depicted in isometric and top view. In Fig. 11b and c the temperature, and the electric potential distribution of the TEG device, exposed to $\Delta T = 25$ K, are illustrated. Under temperature gradients of 25 K and 50 K the voltage outputs

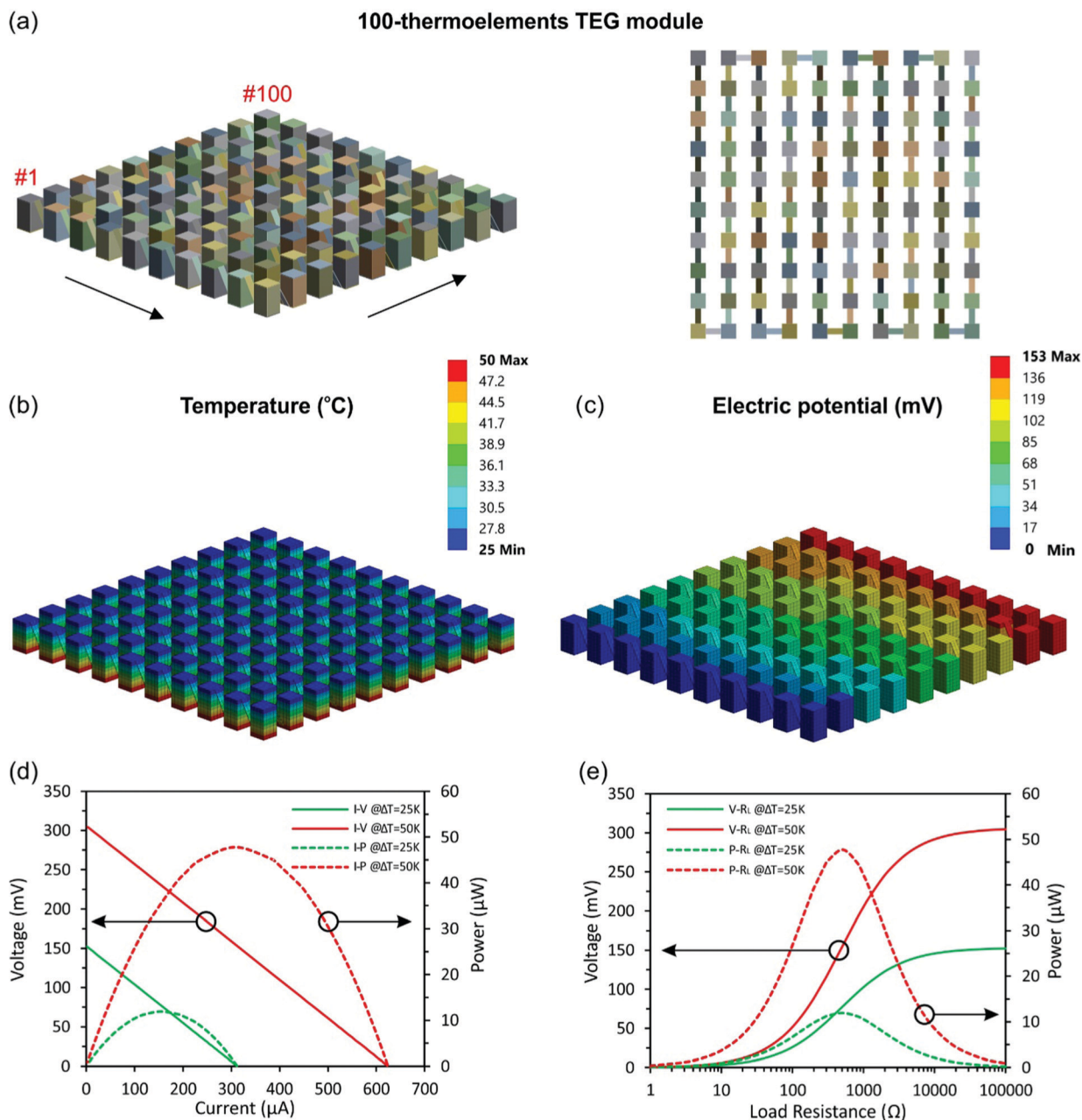


Fig. 11 (a) Geometry of a 100 interconnected thermoelement TEG device, (b) temperature, and (c) electric potential distribution at $\Delta T = 25$ K. (d) $V-I$ and $P-I$ curves, and (e) $V-R_L$ and $P-R_L$ curves.

were 153 mV and 306 mV, respectively. Since the device is equal to 10 interconnected TEG devices, the internal device resistance could be considered as $10 \times R_{\text{TEG}}$. In Fig. 11d and e, $V-I$, $P-I$ curves and $V-R_L$, $P-R_L$ curves are presented. The maximum electrical power output has been estimated to be 11.9 μW and 47.8 μW at 25 K and 50 K, respectively.

3.7 TEG device stability over time

The cementitious TEG device has been tested for its stability and performance over time upon being exposed to a temperature gradient of $\Delta T = 50$ K, the highest gradient to which the TEG device was exposed in this study, for a total duration of 5 hours

(equal to 18000 s). The V_{TEG} and R_{TEG} of the device were monitored over the total duration of the stability experiment as shown in Fig. 12. It could be observed that the electrical characteristics do not change over the whole duration of the stability experiment. Specifically, both the V_{TEG} and R_{TEG} present remarkable stability for $t = 5$ h of device operation in air, which reveals no plausible degradation underlying phenomena *i.e.* (i) cement/SWCNT(0.5) active thermoelectric material oxidation, (ii) oxidation of the Ag-based deposited contacts at the thermoelements “cold” and “hot” sides, due to the particle-consisting Ag-paste nature, or (iii) some possible metal-semiconductor contact loss due to the continuous ΔT exposure for an extended time period,

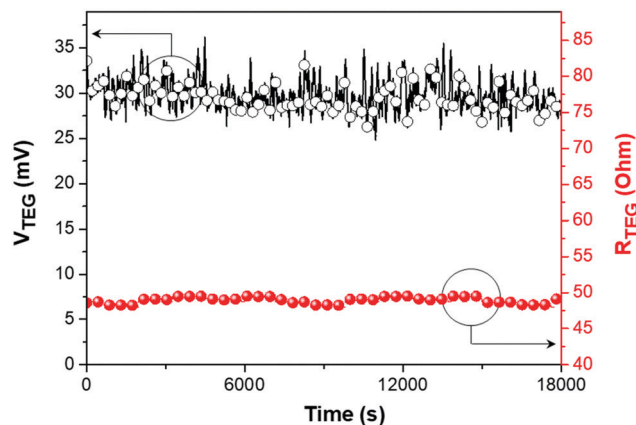


Fig. 12 V_{TEG} and R_{TEG} values of the cement-based TEG device tested for its stability and performance over time, upon being exposed to $\Delta T = 50$ K for 5 h (equal to 18 000 s).

where thermal stresses could destroy the device interface resulting in a dramatic increase of the R_{TEG} .

It is worth mentioning that the structural cement/SWCNT based TEG demonstrated herein is a breakthrough energy harvesting technology for buildings and other civil engineering structures, towards large-scale thermal energy harvesting from existing thermal gradients and “hot-spots” that a large amount of thermal energy is lost to the environment. The harvested energy could be utilised for the realization of various practical applications of the TEG harvested energy, while this study opens the route towards structural TEGs with increased total voltage and power outputs. Some possible applications that can be easily autonomously powered by the TEG energy could be *i.e.*, powering IoT sensors. Specifically, this would require some well-known and commercially available highly integrated DC/DC step-up converters with no additional power requirements, *e.g.*, the LTC3108 (Linear Tech.) that can operate at voltage inputs of at least 20 mV to give an output voltage of 2.2 V or even higher. For instance, utilising the LTC3108, Wei *et al.*⁵³ powered a light-emitting diode (LED) *via* a polymer-based TEG containing 300 pieces of parallelly connected thermocouples (10 in parallel and 30 in series) generating a P_{max} of ~ 50 μW with a V_{OC} higher than 40 mV. In our study, where a cement/SWCNT TEG was realised, already almost 30 mV was produced at $\Delta T = 50$ K. This voltage could be doubled at ~ 60 mV by a simple serial interconnection of two TEG devices, as also predicted by the FEM results.

Finally, the power density of the TEG device can be determined by the following equation (eqn (4)).⁵⁴

$$P_{\text{density}} = \frac{P_{\text{max}}}{N \cdot A} = \frac{(N \cdot S \cdot \Delta T)^2 / 4 \cdot N \cdot \frac{l}{\sigma \cdot w \cdot d}}{N \cdot w \cdot d} = \frac{S^2 \cdot \sigma}{4l} \cdot \Delta T^2 \quad (4)$$

where N is the number of thermoelements, A is the area of the thermoelement, and w , d , and l are the width, thickness, and length of the thermoelements, respectively. The achieved

maximum power density of the cementitious TEG device in our study is 5.02 mW m^{-2} at $\Delta T = 50$ K, giving rise to potentially large scale thermal energy harvesting in buildings *i.e.*, either from ambient thermal energy losses or from solar heated and hot spots generated resulting in temperature gradients. Namely, the power density of this study is the highest ever reported for cementitious thermoelectrics, and specifically three orders of magnitude higher than another study of short carbon fiber cementitious thermoelectric composites (CFRC). Specifically, the authors obtained $\sim 4\text{--}5 \text{ } \mu\text{W}$ of power from one square meter CFRC slab with a thickness of 20 mm, when exposed to a temperature difference of about $60 \text{ } ^\circ\text{C}$, generated under simulated solar irradiation.⁵⁵

4. Conclusions

Cement/SWCNT nanocomposites with p-type thermoelectric characteristics were investigated with respect to their potential use as thermoelectric materials for future energy harvesting applications. Cement/SWCNT nanocomposites demonstrate the highest thermoelectric performance with extremely high values of Seebeck coefficient ($+1348.8 \text{ } \mu\text{V K}^{-1}$) and power factor ($2.89 \times 10^3 \text{ } \mu\text{W m}^{-1} \text{ K}^{-2}$) at a single thermoelement level, compared to other carbon-based cement nanocomposites found in the literature. The cement/SWCNT(0.5) was employed for the fabrication of a TEG device revealing a maximum power output (P_{max}) of $5.02 \text{ } \mu\text{W}$, upon being exposed to a temperature difference (ΔT) of 50 K.

The expected P_{max} considering the experimentally measured Seebeck coefficient at the thermoelement level cannot be reached since ions are consumed in a closed circuit and cannot reach the external circuit. Finite element simulations also confirm the thermoelectric performance of the TEG device.

It can be anticipated that the cement/SWCNT nanocomposites and the cement-based TEG module developed in this work will contribute to the more in-depth understating of the intriguing TE properties of such materials and their ionic thermoelectric character that cannot be realised at the TEG device level, aiming at the large-scale waste thermal energy harvesting by future buildings and other civil engineering structures. It is envisaged that thermoelectric construction and building materials, as well as TEG-enabled ground-breaking concrete structures, will contribute to green construction and reduction of CO_2 emissions through the generation of electrical energy from large amounts of thermal energy losses released in the environment.

Furthermore, utilizing a cement/SWCNT based TEG with a voltage output of 20–50 mV, with or without a step-up converter driving the DC voltage produced in a capacitor, could enable the powering of low-consumption electronic devices integrated in buildings *e.g.*, ultra-low power microcontrollers, wireless sensor networks, *etc.*⁴⁶ To that end, when higher voltage outputs *i.e.*, greater than 100 mV could be achieved, even more sophisticated devices in the new era of Internet-of-Things applications could be powered.⁴⁷

Author contributions

I. V. and L. T. contributed to the conceptualisation and visualization of this work. I. V., L. T., K. T., I. E. K., K. T., and M. L. contributed to the investigation and the methodology of this research work. I. V., L. T., K. T., I. E. K., K. T., M. L., A. E., L. N. G., N.-M. B. and A. S. P. contributed to the data curation, validation, and the formal analysis of the experimental results in this study. I.V. and L.T. wrote the original first draft of this manuscript, while I.V., L.T., K.T., I.E.K., K.T., M.L., A.E., L.N.G., N.M.B. and A.S.P. contributed to the review & editing of the final version of the manuscript. I. E. K., K. T., A. E., and L. N. G. contributed to the development of the theoretical modelling in this work. L. T. and A. S. P. contributed to the funding acquisition, the required resources, the supervision, and the overall project administration.

Conflicts of interest

There are no conflicts to declare.

Acknowledgements

This research has been co-financed by the European Union and Greek national funds through the Operational Program Competitiveness, Entrepreneurship, and Innovation, under the call RESEARCH-CREATE-INNOVATE (HICOTEG-T1EDK-03482).

References

- L. Tzounis, *Advanced Thermoelectric Materials for Energy Harvesting Applications*, IntechOpen, 2019.
- L. Tzounis, M. Petousis, S. Grammatikos and N. Vidakis, *Materials*, 2020, **13**, 2879.
- C. J. Vineis, A. Shakouri, A. Majumdar and M. G. Kanatzidis, *Adv. Mater.*, 2010, **22**, 3970–3980.
- P. Shyni and P. Pradyumn, *RSC Adv.*, 2021, **11**, 4539–4546.
- X.-L. Shi, W.-Y. Chen, X. Tao, J. Zou and Z.-G. Chen, *Mater. Horiz.*, 2020, **7**, 3065–3096.
- R. Freer and A. V. Powell, *J. Mater. Chem. C*, 2020, **8**, 441–463.
- X.-L. Shi, W.-Y. Chen, T. Zhang, J. Zou and Z.-G. Chen, *Energy Environ. Sci.*, 2021, **14**, 729–764.
- W.-Y. Chen, X.-L. Shi, J. Zou and Z.-G. Chen, *Nano Energy*, 2020, **81**, 105684.
- C. R. Gagg, *Eng. Failure Anal.*, 2014, **40**, 114–140.
- U. Berardi and A. A. Gallardo, *Energy Build.*, 2019, **199**, 402–414.
- N. Jaziri, A. Boughamouira, J. Müller, B. Mezghani, F. Tounsi and M. Ismail, *Energy Rep.*, 2019, **6**, 264–287.
- X. Liu, R. Jani, E. Orisakwe, C. Johnston, P. Chudzinski, M. Qu, B. Norton, N. Holmes, J. Kohanoff and L. Stella, *Renewable Sustainable Energy Rev.*, 2020, **137**, 110361.
- S. Ahmad, M. Abdul Mujeebu and M. A. Farooqi, *Int. J. Energy Res.*, 2019, **43**, 1974–2015.
- M. Sun, Z. Li, Q. Mao and D. Shen, *Cem. Concr. Res.*, 1998, **28**, 1707–1712.
- S. Wen and D. D. L. Chung, *Cem. Concr. Res.*, 1999, **29**, 1989–1993.
- S. Wen and D. D. L. Chung, *Cem. Concr. Res.*, 2000, **30**, 661–664.
- S. Wen and D. D. L. Chung, *Cem. Concr. Res.*, 2002, **32**, 821–823.
- S. Wen and D. D. L. Chung, *Cem. Concr. Res.*, 2000, **30**, 1295–1298.
- J. Zuo, W. Yao and K. Wu, *Fullerenes, Nanotubes, Carbon Nanostruct.*, 2015, **23**, 383–391.
- D. Bahar and Y. Salih, *New Carbon Mater.*, 2008, **23**, 21–24.
- T. Ji, X. Zhang and W. Li, *Constr. Build. Mater.*, 2016, **115**, 576–581.
- C. Rudradawong, M. Kitiwan, T. Goto and C. Ruttanapun, *Mater. Today Commun.*, 2020, **22**, 100820.
- J. Wei, Y. Wang, X. Li, Z. Jia, S. Qiao, Q. Zhang and J. Du, *Int. J. Energy Res.*, 2020, **44**, 6885–6893.
- J. Wei, X. Li, Y. Wang, B. Chen, S. Qiao, Q. Zhang and F. Xue, *J. Mater. Chem. C*, 2021, **9**, 3682–3691.
- S. Ghosh, S. Harish, K. A. Rocky, M. Ohtaki and B. B. Saha, *Energy Build.*, 2019, **202**, 109419.
- S. Ghosh, S. Harish, M. Ohtaki and B. B. Saha, *Energy*, 2020, **198**, 117396.
- L. Tzounis, T. Gärtner, M. Liebscher, P. Pötschke, M. Stamm, B. Voit and G. Heinrich, *Polymer*, 2014, **55**, 5381–5388.
- L. Tzounis, M. Liebscher, A. Tzounis, E. Petinakis, A. S. Paipetis, E. Mäder and M. Stamm, *RSC Adv.*, 2016, **6**, 55514–55525.
- M. Liebscher, T. Gärtner, L. Tzounis, M. Mičušík, P. Pötschke, M. Stamm, G. Heinrich and B. Voit, *Compos. Sci. Technol.*, 2014, **101**, 133–138.
- C. K. Mytafides, L. Tzounis, G. Karalis, P. Formanek and A. S. Paipetis, *ACS Appl. Mater. Interfaces*, 2021, **13**, 11151–11165.
- L. Deng, X. Huang, H. Lv, Y. Zhang and G. Chen, *Appl. Mater. Today*, 2021, **22**, 100959.
- Y. Du, J. Xu, B. Paul and P. Eklund, *Appl. Mater. Today*, 2018, **12**, 366–388.
- W.-D. Liu, Y. Yu, M. Dargusch, Q. Liu and Z.-G. Chen, *Renewable Sustainable Energy Rev.*, 2021, **141**, 110800.
- M. Jung, Y.-s. Lee, S.-G. Hong and J. Moon, *Cem. Concr. Res.*, 2020, **131**, 106017.
- L. Tzounis, M. Liebscher, E. Mäder, P. Pötschke, M. Stamm and S. Logothetidis, *AIP Conf. Proc.*, 2015, **1646**, 138–148.
- L. Tzounis, M. Hegde, M. Liebscher, T. Dingemans, P. Pötschke, A. S. Paipetis, N. E. Zafeiropoulos and M. Stamm, *Compos. Sci. Technol.*, 2018, **156**, 158–165.
- J. Wei, Y. Fan, L. Zhao, F. Xue, L. Hao and Q. Zhang, *Ceram. Int.*, 2018, **44**, 5829–5833.
- L. Tzounis, M. Liebscher, R. Fuge, A. Leonhardt and V. Mechtcherine, *Energy Build.*, 2019, **191**, 151–163.
- G. Karalis, L. Tzounis, E. Lambrou, L. N. Gergidis and A. S. Paipetis, *Appl. Energy*, 2019, **253**, 113512.
- M. Matthews, M. Pimenta, G. Dresselhaus, M. Dresselhaus and M. Endo, *Phys. Rev. B: Condens. Matter Mater. Phys.*, 1999, **59**, R6585–R6588.
- R. Fuge, M. Liebscher, C. Schröfl, S. Oswald, A. Leonhardt, B. Büchner and V. Mechtcherine, *Diamond Relat. Mater.*, 2016, **66**, 126–134.

- 42 H. Heise, R. Kuckuk, A. Ojha, A. Srivastava, V. Srivastava and B. Asthana, *J. Raman Spectrosc.*, 2009, **40**, 344–353.
- 43 M. S. Dresselhaus, G. Dresselhaus, R. Saito and A. Jorio, *Phys. Rep.*, 2005, **409**, 47–99.
- 44 M. Liebscher, L. Tzounis, D. Junger, T. T. Dinh and V. Mechtcherine, *Smart Mater. Struct.*, 2020, **29**, 125019.
- 45 Z.-Y. Xiong, B.-Y. Zhang, L. Wang, J. Yu and Z.-X. Guo, *Carbon*, 2014, **70**, 233–240.
- 46 C. Tang, T.-C. Ling and K. H. Mo, *Constr. Build. Mater.*, 2020, **268**, 121079.
- 47 F. Liu and Z. Sun, *Frontiers of Structural and Civil Engineering*, 2016, **10**, 168–173.
- 48 R. Hu, B. A. Cola, N. Haram, J. N. Barisci, S. Lee, S. Stoughton, G. Wallace, C. Too, M. Thomas and A. Gestos, *Nano Lett.*, 2010, **10**, 838–846.
- 49 H. Wang, D. Zhao, Z. U. Khan, S. Puzinas, M. P. Jonsson, M. Berggren and X. Crispin, *Adv. Electron. Mater.*, 2017, **3**, 1700013.
- 50 J. Wei, L. Zhao, Q. Zhang, Z. Nie and L. Hao, *Energy Build.*, 2018, **159**, 66–74.
- 51 D. Zhao, A. Martinelli, A. Willfahrt, T. Fischer, D. Bernin, Z. U. Khan, M. Shahi, J. Brill, M. P. Jonsson and S. Fabiano, *Nat. Commun.*, 2019, **10**, 1–8.
- 52 Q. Jiang, H. Sun, D. Zhao, F. Zhang, D. Hu, F. Jiao, L. Qin, V. Linseis, S. Fabiano and X. Crispin, *Adv. Mater.*, 2020, **32**, 2002752.
- 53 Q. Wei, M. Mukaida, K. Kirihara, Y. Naitoh and T. Ishida, *RSC Adv.*, 2014, **4**, 28802–28806.
- 54 Y. Lu, Y. Ding, Y. Qiu, K. Cai, Q. Yao, H. Song, L. Tong, J. He and L. Chen, *ACS Appl. Mater. Interfaces*, 2019, **11**, 12819–12829.
- 55 J. Wei, Z. Nie, G. He, L. Hao, L. Zhao and Q. Zhang, *RSC Adv.*, 2014, **4**, 48128–48134.